Water Resources Research

RESEARCH ARTICLE
10.1029/2024WR037280

Freezing-Thawing Hysteretic Behavior of Soils

Jidong Teng[1], **Antai Dong**[1,2], **Sheng Zhang**[1], **Xiong Zhang**[2], **and Daichao Sheng**[1,3]

[1]School of Civil Engineering, Central South University, Changsha, China, [2]Civil, Architectural and Environmental Engineering, Missouri University of Science and Technology, Rolla, MO, USA, [3]School of Civil and Environmental Engineering, University of Technology Sydney, Broadway, NSW, Australia

Key Points:

- Supercooling is the primary cause of freezing-thawing hysteresis
- The hysteresis of the soil freezing characteristic curve differs substantively from that of the soil water characteristic curve
- The proposed model can address the impact of supercooling on soil freezing-thawing hysteresis

Correspondence to:

S. Zhang,
zhang-sheng@csu.edu.cn

Citation:

Teng, J., Dong, A., Zhang, S., Zhang, X., & Sheng, D. (2024). Freezing-thawing hysteretic behavior of soils. *Water Resources Research*, *60*, e2024WR037280. https://doi.org/10.1029/2024WR037280

Received 3 FEB 2024
Accepted 14 JUN 2024

Author Contributions:

Conceptualization: Jidong Teng, Antai Dong, Sheng Zhang
Data curation: Jidong Teng, Antai Dong
Formal analysis: Jidong Teng, Antai Dong, Daichao Sheng
Funding acquisition: Jidong Teng
Methodology: Jidong Teng, Antai Dong, Sheng Zhang
Supervision: Sheng Zhang, Daichao Sheng
Validation: Jidong Teng, Antai Dong
Visualization: Antai Dong
Writing – original draft: Jidong Teng, Antai Dong
Writing – review & editing: Jidong Teng, Antai Dong, Xiong Zhang

Abstract The soil freezing characteristic curve (SFCC) plays a crucial role in investigating the soil freezing-thawing process. Due to the challenges associated with measuring the SFCC, there is a shortage of high-quality or rigorous test results with sufficient metadata to be effectively used for applications. Current researchers typically conduct freezing tests to measure the SFCC and assume a singular SFCC when studying the freezing-thawing process of soils, although limited studies indicated that there is a hysteresis during the freezing and thawing process. In this paper, a series of freezing-thawing tests were performed to assess the SFCC, utilizing a precise nuclear magnetic resonance apparatus. The test results reveal a hysteresis between the SFCC obtained from the freezing process and that from the thawing process. Through analyzing the test results, the hysteresis mechanism of the SFCC is attributed to supercooling. Supercooling inhibits initial pore ice formation during freezing, causing a drastic liquid water-ice phase change once supercooling ends. Despite being considered closely related, the hysteresis of the SFCC differs from the soil water characteristic curve (SWCC), and the models used to simulate the hysteresis of SWCC cannot directly be used. To address the impact of supercooling on soil freezing-thawing hysteresis, a novel theoretical model is proposed. Comparisons between the measured and predicted results affirm the validity of the proposed model.

Plain Language Summary Understanding the freezing and thawing behavior of soils is critical for construction in cold regions. The soil freezing characteristic curve (SFCC), which describes the relationship between temperature and unfrozen water content, is essential for characterizing soil behavior during freeze-thaw cycles. However, measuring SFCCs for both freezing and thawing presents significant challenges, often resulting in simplifications and incomplete data in many studies. In this research, we conducted freezing-thawing tests using precise technology called nuclear magnetic resonance to examine the SFCC. We found a hysteresis between the SFCC during freezing and thawing, primarily attributed to supercooling, where the soil remains liquid below the freezing temperature. Supercooling delays initial ice formation, causing a rapid transition from liquid water to ice once it ceases. Importantly, the SFCC hysteresis differs significantly from the drying-wetting hysteresis in the soil water characteristic curve. To address this, we propose a novel model considering the impact of supercooling on soil freezing-thawing hysteresis. The proposed model fits well with the measured data and outperforms existing models. This study introduces a new understanding and a reliable model for soil freezing-thawing process, contributing to better comprehension of frozen soil phase changes.

1. Introduction

The soil freezing characteristic curve (SFCC) is commonly defined as the relationship between subzero temperature and unfrozen water content in soil, which is considered as a constitutive relation for a better understanding of the water-ice phase change in frozen soils (Amankwah et al., 2021; Devoie et al., 2022; K. Sun & Zhou, 2021; Y. Wang & Hu, 2023). The SFCC plays a vital role in predicting hydro-mechanical properties of frozen soils and understanding the mechanism of frost damage in cold regions (Caicedo, 2017; Nishimura & Wang, 2019; Sheng et al., 2014; Teng et al., 2022; Teng, Liu, et al., 2020). Freezing-thawing hysteresis of soil means that the freezing branch of SFCC does not coincide with the thawing branch, that is, the unfrozen water content of freezing process is always greater than the thawing process at a given temperature (Bittelli et al., 2003; Koopmans & Miller, 1966; Nishimura et al., 2021; Pardo Lara et al., 2021). Saberi et al. (2021) showed that the hysteretic nature of SFCC significantly influences ice formation and temperature distribution, which should not be neglected in artificial ground and temporary ground stabilization. In addition, using the thawing branch of SFCC to predict hydro-mechanical properties of the freezing branch, such as frost heave, may lead to a remarkable underestimation. Therefore, a clear physical understanding and mathematical modeling for freezing-thawing hysteresis in soil are of great importance for cold-region geotechnics.

The freezing-thawing hysteretic behavior of soil has been known for a long time. Koopmans and Miller (1966) may be the first ones who observed hysteresis when measuring SFCC of soils in the laboratory. Some experimental investigations have been reported to examine the freezing-thawing hysteretic behavior of soil (Black & Tice, 1989; Fen-Chong & Fabbri, 2005; Morishige & Kawano, 1999; Ren & Vanapalli, 2020). Tian et al. (2014) explained such a mechanism by the difference in ice-water interface curvature during the freezing-thawing process. Watanabe and Osada (2017) found that hysteresis is obvious in a continuous temperature procedure, but it is insignificant at a stepped temperature procedure. Their studies revealed that freezing-thawing hysteresis is essentially attributed to the occurrence of non-equilibrium ice during the freezing process. J. Zhou et al. (2020) found that freezing-thawing hysteresis is strongly related to the supercooling phenomenon. The diversity of these findings indicates that there is no consensus regarding the mechanism of freezing-thawing hysteresis. As a result, SFCCs are often assumed to be a unique curve in numerous common geotechnical and hydraulic applications, and modeling hysteresis in a simple mathematical form is a challenging issue.

Up till now, several potential mechanisms have been reported to explain the freezing-thawing hysteretic behavior of soil. Some studies have adapted mechanisms from drying-wetting hysteresis in unsaturated soils to explain freezing-thawing hysteresis. These mechanisms include: (a) Pore blocking: this explains that liquid water in large pores is delayed from freezing due to blockage by adjacent small pores (Bittelli et al., 2003); (b) Contact angle hysteresis: this displays that the advancing contact angle during thawing is greater than the receding contact angle during freezing (Gharedaghloo et al., 2020); (c) Pore geometry: this explains that the ice-water interface curvature during the freezing process is different from that of the thawing process, particularly in soils with a distinct cylindrical pore composition (Anderson et al., 2009). Additional mechanisms specifically reported for freezing-thawing hysteresis are: (d) Free energy barrier, where the thawing onset temperature is greater than the equilibrium temperature (Petrov & Furó, 2009); (e) Supercooling of pore water: this explains that the pore water remains in a liquid phase until cooling to form stable condensation nodules (Zhang et al., 2020). Although freezing-thawing hysteresis exhibits similarities with drying-wetting hysteresis, there exist essential discrepancies in physics. The ice-water phase change is a thermodynamic phenomenon, while ice can appear anywhere in the pore space that is less affected by pore connectivity and not necessarily the piston-like growth of hydrates. Therefore, mechanisms (a) through (c) cannot be directly applicable to the soil-ice-water system. Mechanisms (d) and (e) postulate ice-water phase change from a thermodynamic point of view, but they are limited in the microscope scale and lack validation. Therefore, the following questions should be deeply considered: *What are the similarities and differences between freezing-thawing hysteresis and drying-wetting hysteresis in physics*? *How can the thermodynamic phenomenon underlying freezing-thawing hysteresis be effectively verified*?

For freezing-thawing hysteresis, various mathematical models have been proposed, which can be classified into three categories. The first category includes empirical models that achieve the best fit for experimental data by adjusting empirical factors (Liu & Yu, 2013; Saberi et al., 2021). While these models heavily rely on experimental data and lack easy generalizability. The second category represents SFCC models developed based on the hysteretic SWCC models, which replace matric suction with temperature by using the Clapeyron equation (Coussy & Fen-Chong, 2005; Fabbri et al., 2009). In such models, some parameters assume identical values for both freezing and thawing curves, reflecting the consistency of basic soil properties during the freezing-thawing process, and avoiding the uncertainty of empirical model calibration. However, these models may not fully capture the nuances of the ice-water phase change, a process involving ice crystal nucleation and growth controlled by supercooling, which is not present in the drying-wetting process. The third category involves thermodynamic models that are established based on discrepancies in thermodynamic behavior during the freezing-thawing process (Petrov & Furó, 2009; Saberi et al., 2021; C. Wang et al., 2018). C. Wang et al. (2018) proposed a hysteresis coefficient to characterize the variability of freezing and thawing points based on the free energy barrier theory, which mainly depends on the micro-pore structure shape of the soil. It is noted that such models focus on individual isolated pores, but soil commonly presents a complex system composed of pores with different sizes and shapes (Teng et al., 2021). *How should the variability in the physical mechanisms of the freezing-thawing and drying-wetting processes be reflected? How can the interactions of ice-water phase changes among different pore sizes be accounted for?* The above-raised questions have not been reasonably answered. Therefore, there is an urgent need to develop a concise and effective model for freezing-thawing hysteresis to address these issues.

This study aims to methodically examine the freezing-thawing hysteretic behavior of soils through a series of laboratory tests on SFCC. The advanced nuclear magnetic resonance (NMR) technique is applied to measure SFCCs of soil samples with different dry densities and initial water contents. To investigate differences between

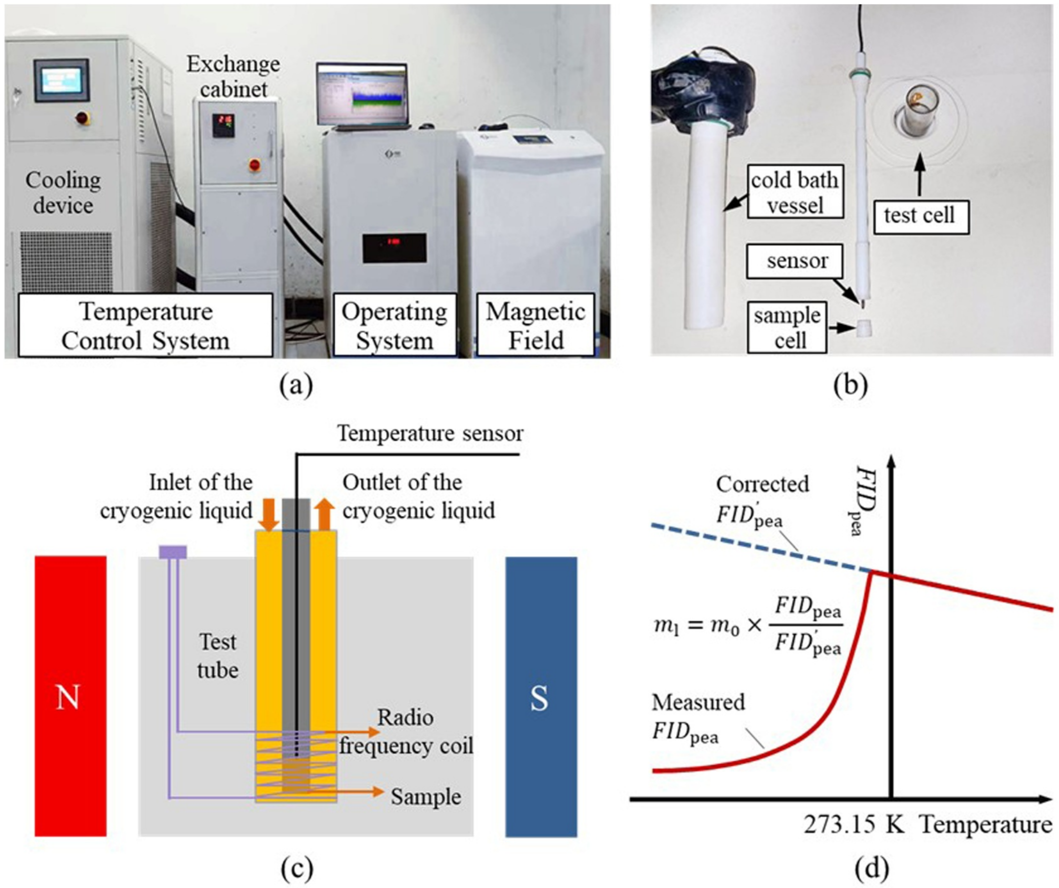

Figure 1. Diagram of nuclear magnetic resonance apparatus: (a) main components, (b) detailed diagram of the test unit, (c) schematic diagram of the test chamber, and (d) Variation of free induction decay peak with temperature.

the hysteretic mechanisms of SFCC and that of SWCC, the scanning curves of SFCC are tested and compared with the main curves using the hysteresis level parameter. Subsequently, a novel SFCC model is developed that comprehensively considers the entire freezing-thawing process. The rationality and effectiveness of the proposed model are then validated. The experimental and theoretical investigation in this study may provide insights into a better understanding of the freezing-thawing hysteretic mechanism.

2. Experimental Study

2.1. Test Equipment, Materials, and Procedure

The laboratory tests are performed using the NMR Geotechnical Microstructure Analyzer (NMRC12-010V), which is jointly developed by Central South University and Suzhou Niumag Analytical Instrument Corporation. The apparatus consists of three parts: an operating system, a magnetic field, and a temperature control system (see Figure 1a). The operating system is utilized to set test parameters and record experimental data. The magnetic field is used for magnetization, resonance, and relaxation of hydrogen protons. The temperature control system controls the sample temperature, including the exchange cabinet and chiller. The detailed diagram of the test unit is shown in Figure 1b, whereby a cylindrical sample of 9 mm in diameter and 10 mm in height can be placed inside the sample cell. A temperature sensor is placed at the top of the sample to record temperature changes in real-time. The test cell and the cold bath vessel are sealed with a sealing film to prevent external water vapor from affecting the test. The entire test section is wired to the control system to record NMR signal values for subsequent data processing. The apparatus can precisely control temperature with an accuracy of 0.1 K from 243.15 to 363.15 K. Notably, temperature control and magnetization are executed within the magnetic field, mitigating secondary disturbances caused by sample transfer for temperature adjustments. This system, characterized by precise

Table 1
Physical Properties of the Experiment Materials

Soil type	Specific gravity	Liquid limit (%)	Plastic limit (%)	Optimum water content (%)	Maximum dry density (g/cm^3)
Poorly graded sand	2.65	/	/	/	1.65
Silt	2.69	23.18	19.56	14.20	1.90
Fat clay	2.69	57.0	26.00	15.31	1.82

temperature control, non-destructive sample structure, and user-friendly operation, facilitates accurate measurement of unfrozen water content.

Figure 1c illustrates the schematic representation of the test chamber. The magnetic field, generated by the spin of hydrogen nuclei, aligns with the external magnetic field, resulting in a macroscopic longitudinal magnetization vector. Subsequently, the radio frequent (RF) coil emits a pulse to excite proton resonance, altering the rotation direction of hydrogen nuclei. This process can reduce the macroscopic longitudinal magnetization vector to zero, generating a maximum transverse magnetization vector, and inducing a voltage in the receiving coil. Upon removal of the RF field, hydrogen nuclei gradually return to the initial state. As the longitudinal magnetization vector reaches its maximum magnitude, the transverse magnetization vector magnitude decreases until vanishes. The voltage produced by the receiver coil decreases over time during relaxation, which is defined as free induction decay (FID). The ratio of the peak FID to the mass of liquid water (m_l) at the same temperature is constant. This constant varies linearly with temperature. Figure 1d illustrates the variation of FID peak ($\mathrm{FID_{peak}}$) with temperature. The solid red line in the positive temperature region exhibits a linear increase in FID peak as the temperature decreases, where the mass of liquid water remains constant ($m_l = m_0$). The dashed blue line presents the case assuming no phase change, that is, m_l remains equal to m_0., which is determined by a linear extension from the positive temperature region. As the liquid water gradually freezes with decreasing temperature, the measured FID peak follows the solid red line. In negative temperatures, the ratio of the measured FID peak ($\mathrm{FID_{peak}}$) to the correct value ($\mathrm{FID'_{peak}}$) is equal to the ratio of m_l to m_0. Therefore, the mass of liquid water can be determined as $m_l = m_0 \times \mathrm{FID_{peak}}/\mathrm{FID'_{peak}}$, and the volume unfrozen water content is obtained by calculating the ratio of liquid water volume to the total volume of the soil sample.

Three types of soils were selected as test materials: poorly graded sand, primarily composed of quartz with a grain size ranging from 0.075 to 1.0 mm; silt sampled from Hohhot Baita International Airport; and fat clay sampled from Nanning City in Guangxi Province, China. The basic physical properties are presented in Table 1, and particle size distribution curves are shown in Figure 2. The samples for NMR tests were prepared as follows: the oven-dried soil material underwent a sieving process using a 1 mm round-hole sieve. They were then mixed with a specified amount of distilled water to achieve the target initial water contents. The samples were subsequently compacted to the target dry density. Additional saturation procedures were conducted for saturated samples. Subsequently, a sample measuring 9 mm in diameter and 10 mm in height was extracted from a specially designed NMR sampler. The remaining soil was then dried to determine the actual water content.

Twelve conditions were designed to investigate the freezing-thawing hysteretic behavior, as outlined in Table 2. Samples in all cases underwent the main freezing-thawing process with temperatures ranging from 248.15 to 283.15 K. The main freezing process from 272.15 to 266.15 K was encrypted into 0.5 K temperature intervals, resulting in 23 representative temperature points. Similarly, the main thawing process from 270.15 to 273.15 K was also encrypted into 0.5 K temperature intervals, resulting in 20 representative temperature points. Samples in cases 4, 8, and 12 were cooled down to 265.15 K after the main freezing-thawing process and then subjected to a scanning freezing-thawing process over the temperature range from 265.15 to 272.15 K. Unlike the main freezing-thawing, where a complete freezing or thawing state can be achieved, neither freezing nor thawing is thoroughly completed during the scanning freezing-thawing process. The temperature

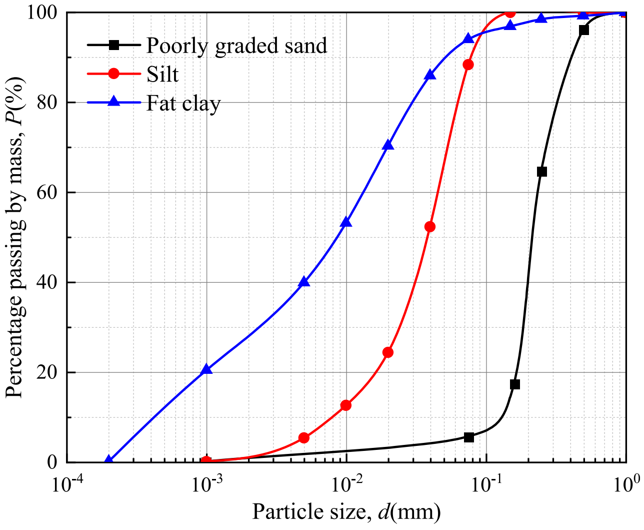

Figure 2. Particle size distribution curves of the experiment materials.

Table 2
Test Conditions

Case	Soil type	Dry density (g/cm^3)	Designed water content (g/g)	Measured water content (g/g)	Temperature mode
1	Poorly graded sand	1.4	0.10	0.092	Main freezing-thawing process
2		1.4	0.15	0.154	
3		1.4	0.15	0.230 (Saturated)	
4		1.6	0.15	0.196 (Saturated)	Main freezing-thawing process and Scanning process
5	Silt	1.6	0.10	0.108	Main freezing-thawing process
6		1.6	0.20	0.207	
7		1.6	0.15	0.276 (Saturated)	
8		1.8	0.15	0.237 (Saturated)	Main freezing-thawing process and Scanning process
9	Fat clay	1.6	0.10	0.102	Main freezing-thawing process
10		1.6	0.20	0.203	
11		1.6	0.15	0.329 (Saturate)	
12		1.8	0.15	0.263 (Saturate)	Main freezing-thawing process and Scanning process

procedures for the two freezing-thawing processes are illustrated in Figure 3. Each temperature point was maintained for 30 min to ensure an equilibrium state. After the tests, the signal data from the samples were analyzed and processed to obtain the unfrozen water content at each temperature.

2.2. Experimental Results and Analysis

2.2.1. Hysteresis of Main Curves

The measured results of cases 3, 7, and 11 are selected to investigate the freezing-thawing hysteretic behavior of three saturated soils during the main freezing-thawing process, as shown in Figure 4. The SFCC of the main freezing process exhibits three stages: the supercooling stage, rapid decline stage, and residual stable stage. The pore water remains unfrozen in the supercooling stage, then freezes rapidly with the disappearance of supercooling, and eventually stabilizes gradually. Similarly, the SFCC of the main thawing process undergoes three stages: the stable stage, slow thawing stage, and fast thawing stage. Unlike the freezing process, the supercooling phenomenon is not observed during thawing. Supercooling refers to the phenomenon that a material remains liquid below its freezing point due to the absence of stable nuclei (Style et al., 2011). As the soil temperature continues to decrease, the nucleation barrier is broken, stable nuclei are configured, and the supercooling phenomenon disappears. The temperature at which supercooling disappears during the freezing process is defined as the supercooling temperature (T_{sc}), whereas the temperature at which the ice crystals completely thaw during the thawing process is define as the thawing temperature (T_m). The supercooling temperature is considerably lower than the thawing temperature, resulting in a delayed phase change caused by pore water supercooling.

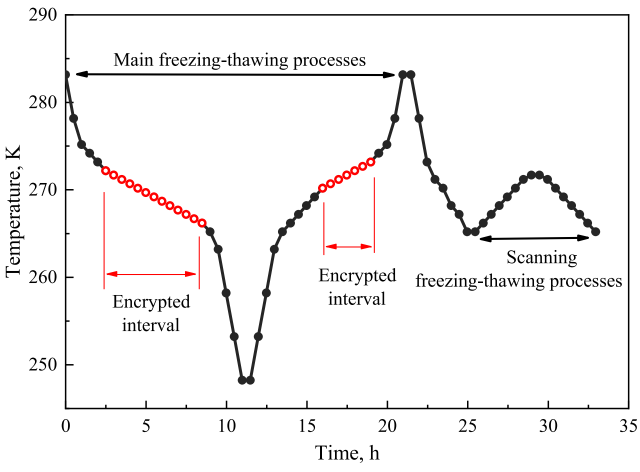

Figure 3. Temperature-time series for the nuclear magnetic resonance experiment.

In Figure 4, the main freezing-thawing curves exhibit hysteresis predominantly during the supercooling and rapid decline stages of the process, with less apparent hysteresis during the residual stable stage. Thus, a hysteretic loop can be plotted based on the T_m point, T_{sc} point, the intersection of decline branches of the freezing-thawing curve, and the intersection of the last two stages of the thawing curve as vertices. The hysteretic loops are mainly indicative of the fact that the three soils show hysteresis. The hysteresis loops of the three soils displayed a characteristic shape with a wider top and narrower bottom, especially in fat clay and silt. The difference in shape is primarily attributed to the more widely distributed pore sizes in silt and clay, which result in a slower rate of SFCC during thawing compared to sand.

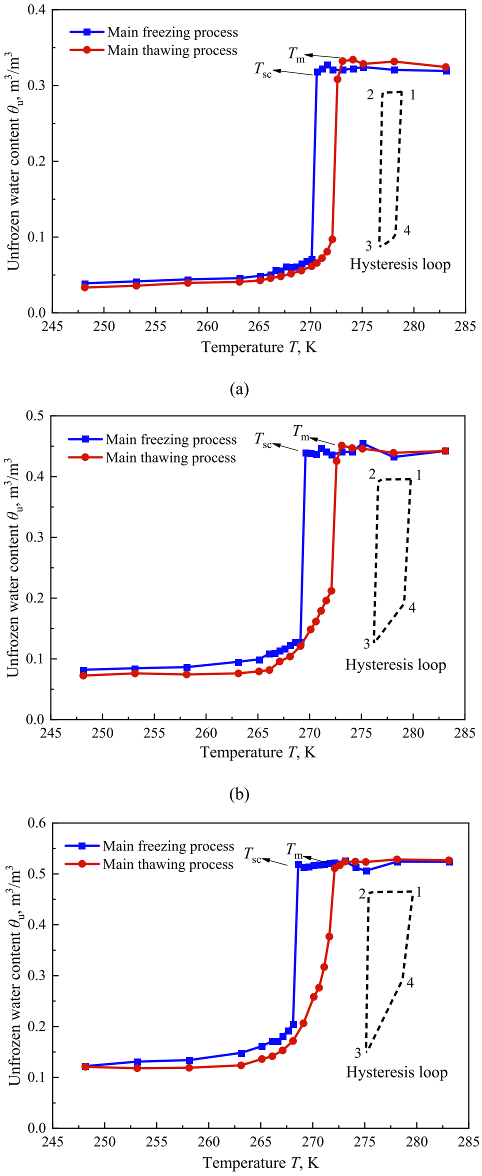

(a)

(b)

(c)

Figure 4. SFCCs during the main freezing-thawing process: (a) Case 3, (b) Case 7, (c) Case 11.

Comparing the SFCC slopes between freezing and thawing curves, the overall decrease rate of the freezing branch is greater than that of the thawing branch. Once the soil temperature below than T_{sc}, the freezing curve drops rapidly, while the thawing curve rises slowly overall and accelerates only when approaching T_m. It is noted that this phenomenon differs from the approximate parallelism observed in SWCCs between drying and wetting curves (Fu et al., 2021; Zhai et al., 2020). It indicates that freezing-thawing hysteresis cannot be explained by directly using the SWCC hysteresis. The freezing of pore water requires two conditions: nucleation nuclei and the Gibbs-Thomson effect. Generally, nucleation nuclei are the prerequisite for freezing, whereas the Gibbs-Thomson effect determines the order of freezing. As a rule, a smaller pore corresponds to a lower freezing temperature. During the supercooling stage, due to the absence of consideration nuclei, liquid water in large pores is unable to freeze even when reaching the phase change temperature determined by the Gibbs-Thomson effect. Only when nucleation nuclei form and the supercooling state ends, does the suppressed pore water freeze rapidly. It then propagates nucleation nuclei to adjacent small pores through the ice-water interface, triggering their freezing and accelerating the overall freezing speed. This phenomenon is analogous to the immediate freezing of table water taken from a refrigerator and shake. The main dissimilarity is that it results from a shock wave disrupting the supercooling state rather than a cooling effect. It indicates that freezing-thawing hysteresis is the result of thermodynamic phase change, particularly influenced by the supercooling process.

2.2.2. Effect of the Dry Density

The measured values of cases 3 & 4, 7 & 8, and 11 & 12 are selected to examine the effect of dry density on freezing-thawing hysteresis, as demonstrated in Figure 5. The T_{sc} values of poorly graded sand with dry densities of 1.4 and 1.6 g/cm^3 are 270.65 and 271.15 K, respectively, while their T_m values are almost the same and close to 273.15 K. As for silt and fat clay, the influence of two different dry densities, 1.6, and 1.8 g/cm^3, on the phase change temperatures T_{sc} and T_m cannot be easily distinguished. It indicates that variations in dry density within this range may not lead to significant shifts in phase change temperatures.

The influence of dry density on freezing-thawing hysteresis is mainly reflected in the unfrozen water content at the initial and residual stages. Figure 5 shows that increasing dry density leads to a decrease in the unfrozen water content at the initial stage, coupled with an increase at the residual stage. It can be mainly attributed to the reduction in overall pore volume with increasing dry density, leading to a decrease in the initial saturated water content. Meanwhile, the decrease in overall pore size amplifies the proportion of adsorbed water, contributing to an increase in the unfroze water content at the residual stage. From the hysteretic loops in Figure 5, it is observed that smaller dry densities exhibit greater height in their hysteretic loops, encompassing hysteretic loops of larger dry densities. It suggests that the hysteretic degree becomes weakened in soils with larger dry densities.

2.2.3. Effect of the Initial Water Content

The effect of the initial water content on freezing-thawing hysteresis is shown in Figure 6. It can be observed that a higher initial water content corresponds to a lower value of T_{sc}. The pores occupied by liquid water become larger with increasing initial water content. According to the Gibbs-Thomson effect, the phase change temperature should be higher in theory. However, the measured results obviously exhibit contradictory outcomes. The primary reason may be that when the pore water is supercooled, the soil system remains in a sub-stable state and no longer satisfies the thermodynamic equilibrium state required by the Gibbs-Thomson effect. The T_m remains nearly

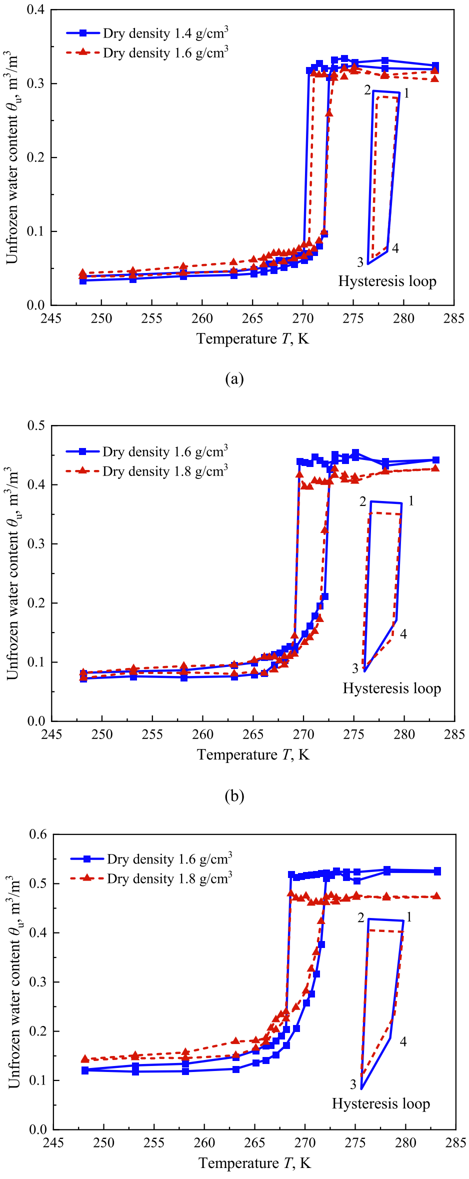

(a)

(b)

(c)

Figure 5. Effect of various dry densities on SFCCs: (a) Cases 3 & 4, (b) Cases 7 & 8, and (c) Cases 11 & 12.

constant between 272.65 and 273.15 K, regardless of the variations in the initial water content. The SFCC slope of the thawing branch rises with the increasing initial water content. This is because the additional water increases the proportion of capillary water. The ice-water phase change in the capillary zone is more temperature-sensitive than that in the adsorption zone. Therefore, the effects of initial water content are completely different during freezing and thawing. The freezing process is primarily influenced by supercooling, while the thawing process relies on the pore structure and water storage state.

The initial water content possesses a different impact on SFCCs during freezing and thawing, which will influence the freezing-thawing hysteretic behavior of soils. The hysteretic level (ΔS_u) is defined as the initial water content divided by the difference in unfrozen water content between the freezing and thawing at the same temperature, expressed as $\Delta S_u = (\theta_{\mathrm{uF}} - \theta_{\mathrm{uT}})/\theta_0$. The variation of hysteretic level (ΔS_u) versus temperature is shown in Figure 7. ΔS_u initially rises with decreasing temperature, peaking near T_{sc}, and then drops. The temperature range for the rise in ΔS_u is greater than that of the drop, which indicates that supercooling leads to a more intense ice-water phase change in the post-supercooling stage. As the initial water content decreases, the temperature corresponding to the peak value of ΔS_u increases, while the peak value of ΔS_u decreases, which means freezing-thawing hysteresis becomes insignificant. Particularly, the hysteresis of fat clay with an initial water content of 0.163 m^3/m^3 is insignificant, as shown in Figure 7c. This may be attributed to the predominance of liquid water in the form of adsorbed water when the liquid water content is low, while hysteresis mainly occurs in the capillary zone. Therefore, a higher initial water content will result in a more significant freezing-thawing hysteresis.

2.2.4. Effect of the Temperature Mode

The measured results associated with cases 4, 8, and 12 are here chosen to investigate the effect of temperature mode on freezing-thawing hysteresis, as shown in Figure 8. The plotted results reveal that the scanning thawing curve approximately follows the path of the main thawing curve. The scanning freezing curve is slightly higher than the scanning thawing curve. It is noted that there is no supercooling stage in the scanning freezing curve, despite its starting temperature (272.15 K) is set higher than T_{sc}. This is because the soil is not completely melted at the end of the previous, and the residual ice crystals inside are able to eliminate supercooling by providing ice nuclei. Conversely, if the melting process ends at a temperature above the T_m, the ice in the soil will be completely melted and the supercooling will be present in the subsequent freezing process, but this is essentially already a main freezing-thawing process.

The variation of the hysteretic level versus temperature for both the main and scanning freezing-thawing processes is shown in Figure 9. The hysteretic level of the main process exhibits a unimodal pattern, with maximum values exceeding 0.5 for all three soils and being the largest for poorly graded sand. The reason may be that the pore size distribution of poorly graded sand is more concentrated, resulting in steeper and parallel SFCCs during freezing and thawing. The hysteretic level of the scanning process is very low, with the maximum values lower than 0.1 for all three soils. This fact indicates that the hysteretic behavior during the scanning process is less significant than that during the main process. Moreover, the absence of supercooling during the scanning freezing process is the main reason for the insignificant hysteresis.

Some factors may have specific impacts on freezing-thawing hysteresis, such as pore blocking, pore geometry effect, and free energy barrier. During the drying-wetting process, the water-gas interface propagates

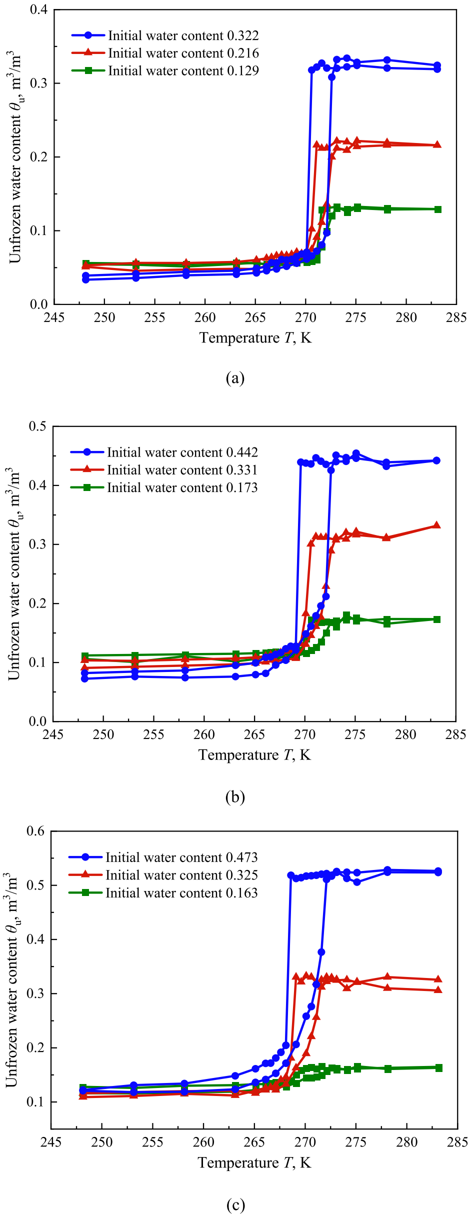

Figure 6. Effect of various initial water contents on SFCCs: (a) Cases 1–3, (b) Cases 5–7, and (c) Cases 9–11.

unidirectionally from the surface in contact with the atmosphere, and small pores adjacent to large pores may block the water-gas interface (Zhai et al., 2020). However, an analogous situation does not exist during the freezing-thawing process. In the main freezing-thawing process, ice crystals may initially from in large pores at any location within the soil and not necessarily at locations in contact with atmosphere. During the scanning freezing-thawing process, incompletely melted ice crystals are distributed at multiple locations within the soil pores, and the ice-water interface propagates from these locations toward nearby areas. This multi-start and multi-directional propagation weaken the effect of pore blocking on hysteresis, which is another reason for the insignificant hysteresis during the freezing-thawing process. The pore geometry effect and free energy barrier can explain freezing-thawing hysteresis by the constant difference between the freezing point and the thawing point. However, the difference in Figure 9 is not constant but decreases with the freezing of liquid water. Thus, it can be concluded that supercooling is the primary reason for freezing-thawing hysteresis. Additionally, it is necessary to consider freezing-thawing hysteresis in the main process, while the hysteresis during the scanning process is not significant due to the absence of supercooling. It further implies that approximating the scanning curves with the main thawing curve results in only very minor errors, which provides a clear and concise insight into the application of SFCC hysteresis.

3. Theoretical Analysis

3.1. Pore Water Supercooling

Classical nuclear theory suggests that pore water in supercooling is metastable, and freezing is only able to begin after breaking the nucleation barrier and forming stable condensation nuclei (Fletcher, 1958; Petrov & Furó, 2009; Wan et al., 2020). As shown in Figure 10, the phase change of pore water during soil freezing can be divided into five stages, AB stage, where pore water remains unfrozen at a temperature above T_{eq}; BC stage, where pore water is supercooled and forms unstable ice embryos; CD stage, where supercooling ends with the formation of stable nuclei, and the release of latent heat raises the temperature back to T_{eq}; DE stage, where ice nuclei in free water steadily grow into ice crystals; EF stage, where capillary and adsorbed water freeze, causing the temperature to further drop. This indicates that the soil temperature reaching T_{sc} implies the breaking of the nucleation barrier and the initiation of freezing of pore water. Importantly, the fact that T_{sc} is lower than T_{eq} determines the presence of freezing-thawing hysteresis.

The surface of soil particles can provide many nucleation sites; thus, the phase change of soil pore water belongs to heterogeneous nucleation. The heterogeneous nucleation substrates are classified as planar, convex, and concave according to their surface geometrical properties. Qian and Ma (2009) numerically verified that the effect of different shape substrates no longer produces significant differences when the ratio of nucleation matrix to nucleation nodule size is greater than 5. The radius of condensation nodules is generally taken to be 0.1 μm or smaller, while the particle size of soil particles is generally taken in the range of 1–100 μm (Kowalenko & Babuin, 2013; To et al., 2018), which is much greater than the nucleation size. Therefore, the nucleation on the surface of soil particles could be reduced to heterogeneous nucleation on a planar substrate. The schematic diagram of the heterogeneous nucleation on a planar substrate is presented in Figure 11.

Assuming a spherical-crowned ice embryo with a radius (r_i), the free energy change (ΔG) resulting from the formation of the ice embryo can be stated by (Kurz & Fisher, 1992):

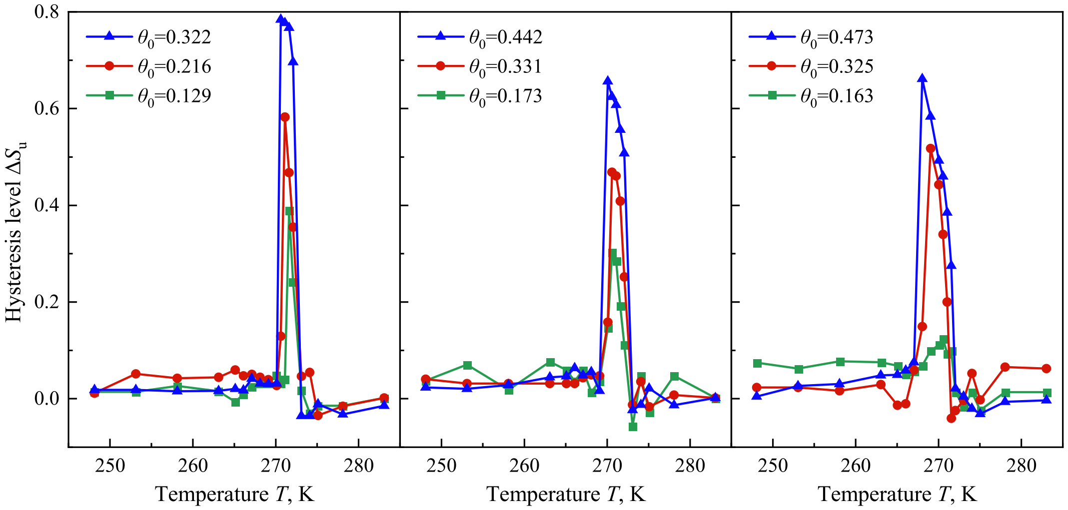

(a) (b) (c)

Figure 7. Variation of hysteresis level versus temperature at various initial water contents: (a) Cases 1–3, (b) Cases 5–7, and (c) Cases 9–11.

$$\Delta G = \Delta G_v + \Delta G_s = \Delta g V_i + \sigma_{il} A_{il} + (\sigma_{si} - \sigma_{sl}) A_{si} \tag{1}$$

where ΔG_v and ΔG_s represent the contributions of volume and area terms to the system's free energy, respectively (J); Δg denotes the difference in free energy per unit volume between ice and liquid (<0, J/m^3); V_i is the volume of the ice embryo (m^3); σ_{xy} and A_{xy} are the surface energy (J/m^2) and surface area (m^2), respectively, between different phases. Their subscripts s, i, and l represent substrate, ice, and liquid, respectively.

The nucleation energy required to overcome the nucleation barrier can be calculated by determining the extremum of Equation 1, that is, solving for $d(\Delta G)/dr_i = 0$. Additional details are provided in Appendix A.

$$\Delta G_b = \frac{16}{3} \pi \sigma_{il}^3 \left(\frac{N_A \Omega_s T_{\mathrm{eq}}}{L_{wi} \Delta T} \right)^2 f(\theta) \tag{2}$$

where ΔG_b denotes the Gibbs free energy breaking nucleation barrier (J); σ_{il} is the surface energy between ice and water (J/m^2); N_A is Avogadro's constant (1/mol); Ω_s is the volume of a single water molecule (m^3); L_{wi} is the latent heat released by water freezing (J/mol); ΔT is the difference between the equilibrium temperature and system temperature, expressed as $\Delta T = T_{\mathrm{eq}} - T$ (K); T_{eq} is the equilibrium temperature; $f(\theta)$ is the geometric factor of the substrate surface, expressed as $f(\theta) = (2 + \cos\theta)(1 - \cos\theta)^2/4$; θ is the contact angle between the ice embryo and substrate.

The nucleation barrier directly determines the rate of nucleation nuclei formation. The number of condensation nuclei formed per unit time and unit volume is defined as the nucleation ratio (J),

$$J = K \exp\left(-\frac{\Delta G_b}{kT} \right) \tag{3}$$

where K denotes the nucleation rate factor, related to the atomic migration rate and approximately in the range of 10^{36}–10^{42} (1/(m$^3 \cdot$ s)), and k is the Boltzmann constant (J/K). Substituting Equation 2 into Equation 3 yields:

$$J = K \exp\left(-\frac{16\pi T}{3k} \left(\frac{N_{\mathrm{A}} \Omega_{\mathrm{s}}}{L_{\mathrm{wi}} \Delta T} \right)^2 \sigma_{\mathrm{il}}{}^3 f(\theta) \right) \tag{4}$$

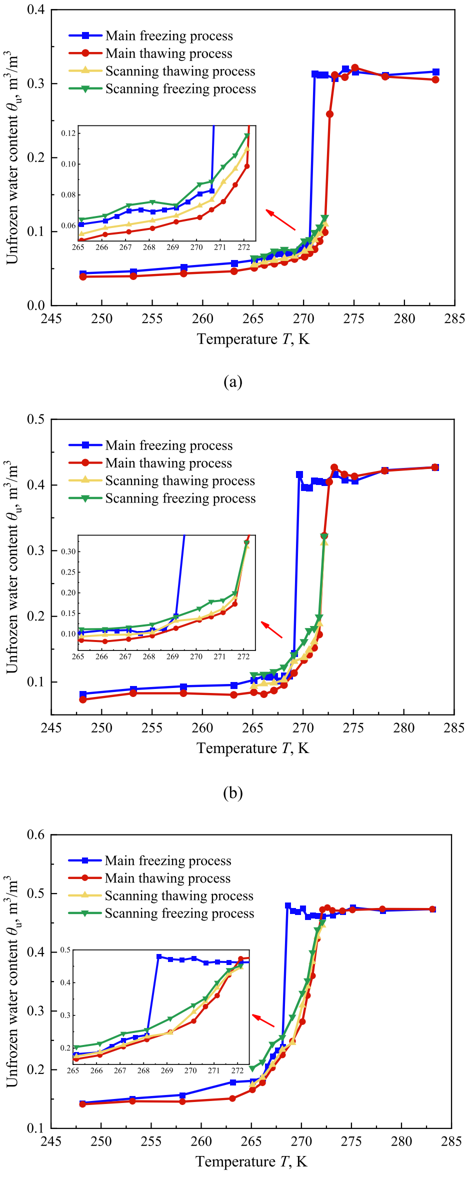

(a)

(b)

(c)

Figure 8. SFCCs associated with the main and scanning freezing-thawing processes: (a) Case 4, (b) Case 8, and (c) Case 12.

According to the classical nucleation theory, the nucleation barrier can only be overcome when temperature (T) drops to supercooling temperature ($T_{\rm sc}$), resulting in an increase in nucleation ratio (J) from 0. ΔT is currently defined as the supercooling degree ($\Delta T_{\rm sc}$), $\Delta T_{\rm sc} = T_{\rm eq} - T_{\rm sc}$. The impact of freezing rate and soil volume on the probability of ice formation is much smaller compared to the contact angle (Z. Sun & Scherer, 2010; Wan et al., 2020, 2022), and thus, $\Delta T_{\rm sc}$ is primarily determined by the contact angle (θ). Fletcher (1958) and Mullin (2001) suggested that nucleation becomes considerable when J reaches 1 (1/(cm^3·s)), corresponding to the case of $\Delta T = \Delta T_{\rm sc}$,

$$\Delta T_{\rm sc} = \frac{N_A \Omega_s}{L_{\rm wi}}\left[\frac{16\pi T \sigma_{il}{}^3}{3k\ln(K)}\right]^{1/2} f(\theta)^{1/2} \tag{5}$$

The specific parameters in Equation 5 can be obtained from Table 3, and the variation of $\Delta T_{\rm sc}$ in terms of θ has been plotted in Figure 12. The results show that $\Delta T_{\rm sc}$ increases with the rise of θ, while the extensive variation of K has a negligible impact on $\Delta T_{\rm sc}$.

By substituting the parameter values from Table 3 into Equation 5, it can be further simplified as follows:

$$\Delta T_{\rm sc} = 32.51 f(\theta)^{1/2} \tag{6}$$

where the factor 32.51 results from the calculation of parameters in Table 3, and K is taken as 10^{39} (1/(m^{3}s)). The contact angle is a key factor determining $\Delta T_{\rm sc}$, which depends on the physicochemical properties of soil particle surfaces (Gharedaghloo et al., 2020). In instances where the bonding energy between soil surface and ice crystal is low and lattice matching occurs, the surface energy between soil and ice, as well as the value of θ, tends to be small (Fletcher, 1958). Due to the small volumes and irregular surface shapes of soil particles, direct experimental measurement of θ is challenging. It is mainly determined through back-calculation based on classical nucleation theory (Bachmann et al., 2003). Ying et al. (2021) proposed that soil, as a hydrophilic material, has a small contact angle, and the fitting result for Lanzhou silt is 21.3°. Kulkarni et al. (2012) indicated that the contact angle of mineral particles generally falls between 18° and 24°. Wan et al. (2022) suggested that the contact angle during nucleation is related to pore size, with sand having larger pores exhibiting a smaller contact angle compared to clay, resulting in higher nucleation efficiency. Based on the above studies, it is recommended to consider contact angle ranges for different soil types as follows: 14°–22° for sand, 18°–26° for silt, and 20°–28° for clay.

3.2. Freezing-Thawing Hysteresis Model

3.2.1. Basic Assumptions

To develop a new SFCC hysteresis model, some assumptions are made as follows:

1. The soil is assumed to be saturated, that is, the air phase within voids is neglected.
2. The soil pores are regarded as a collection of capillary tubes with varying sizes arranged in descending order: $r_0, r_1, r_2, \ldots, r_{\min}$.
3. The thawing process is assumed to be approximately equivalent to the wetting process of unsaturated soil.

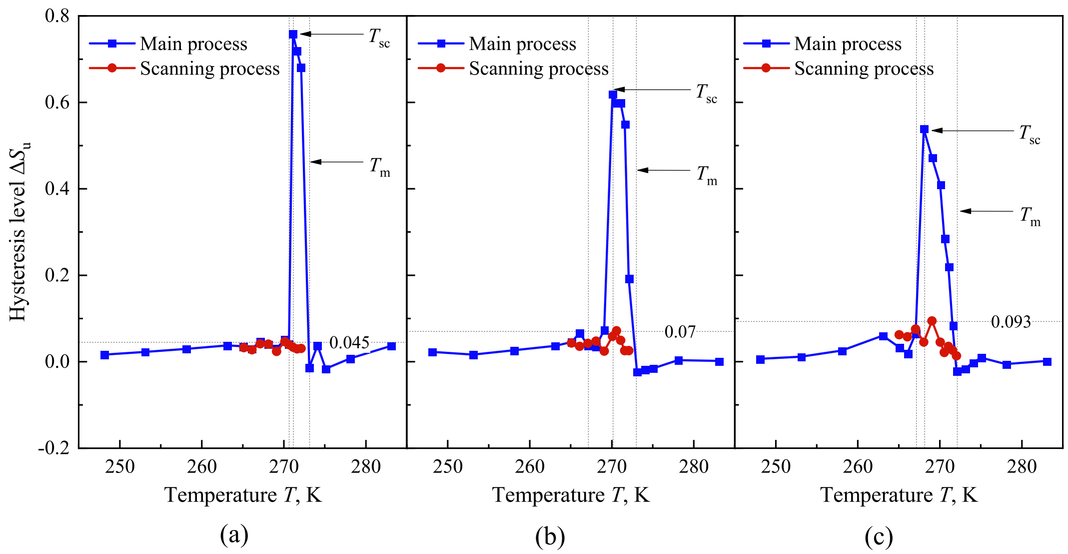

Figure 9. Variation of the hysteresis level in terms of the temperature during the main and scanning freezing-thawing processes: (a) Case 4, (b) Case 8, and (c) Case 12.

3.2.2. The SFCC During the Thawing Branch

The thawing process in soil lacks a "superheated" state analogous to supercooling, and the physical process of thawing is relatively straightforward. The SFCC during the thawing branch is first considered, which is established by combining SWCC models and the Clapeyron equation based on the similarity between the wetting process of unsaturated soils and the thawing process of frozen soils. Commonly used SWCC models include the BC model (Brooks & Corey, 1964), the VG model (Van Genuthern, 1980), and the FX model (Fredlund & Xing, 1994), among others. Prioritizing the smoothness, closure, and simplicity in expressions, the VG model is chosen to establish the SFCC during the thawing branch.

The expression of the VG model is as follows:

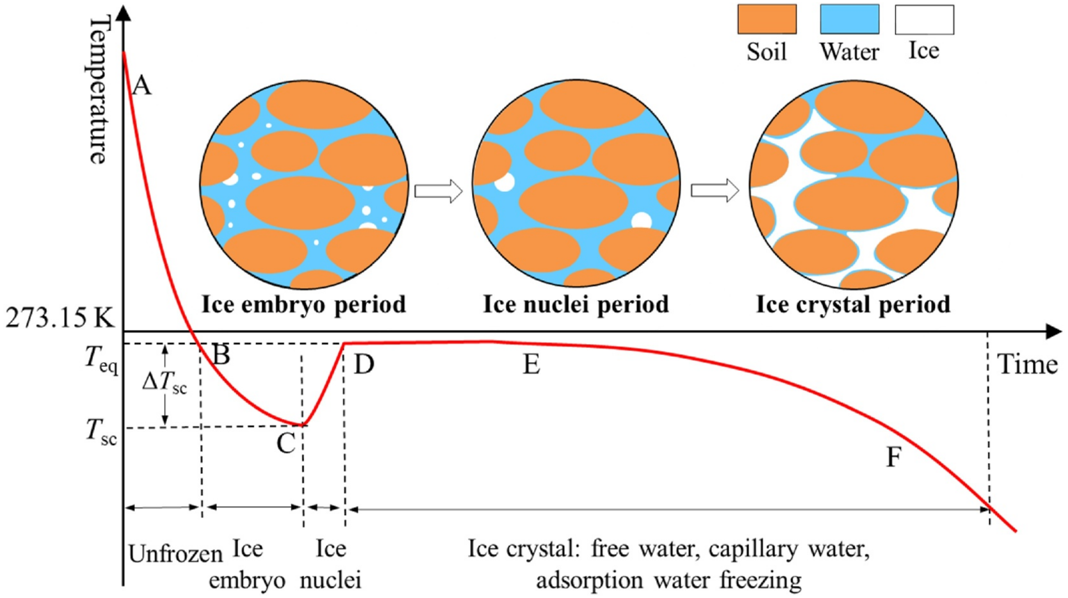

Figure 10. Temperature characteristic curve of the soil freezing process.

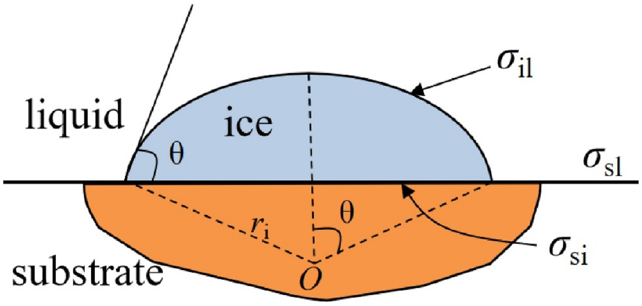

Figure 11. Schematic representation of the heterogeneous nucleation on a planar substrate.

$$\theta_w = \theta_r + (\theta_s - \theta_r)\left[\frac{1}{1 + (\alpha\psi)^n}\right]^m \tag{7}$$

where θ_w denotes the volume water content (m^3/m^3); θ_s represents the saturated water content (m^3/m^3); θ_r is the residual water content (m^3/m^3); ψ is suction (kPa); α, m, and n are the fitting parameters of the VG model, where α is the reciprocal of the air entry value (1/kPa),

$$\alpha = \frac{1}{\psi_\alpha} \tag{8}$$

where ψ_α is the suction when air enters during the wetting process (kPa).

The equilibrium relationship between temperature and suction in frozen soils is described by the Clapeyron equation. Kurylyk and Watanabe (2013) demonstrated that, although there are variable forms of the Clapeyron equation, the choice of equation form has little impact for temperatures greater than 263.15 K. In the current investigation, among various forms, a linear function is chosen as follows:

$$\psi = H_f \rho_w \frac{T_0 - T}{T_0} \tag{9}$$

where H_f denotes the latent heat of phase change per unit mass of liquid (J/kg); ρ_w is the density of liquid water (kg/m^3); and T_0 represents the freezing temperature of bulk water (K).

When applying the SWCC model to the SFCC model under negative temperature, θ_w corresponds to the unfrozen water content during the thawing process (θ_{uT}), θ_r represents the residual unfrozen water content, and ψ_α corresponds to the matric suction at the T_m (ψ_m), which can be obtained from Equation 9 at T_m.

$$\psi_m = H_f \rho_w \frac{T_0 - T_m}{T_0} \tag{10}$$

Through combining Equations 6–9, the SFCC during the thawing branch is expressed as,

$$\begin{aligned}\theta_{\mathrm{uT}} &= \theta_r + (\theta_s - \theta_r)/\left[1 + \left(\frac{T_0 - T}{T_0 - T_{\mathrm{m}}}\right)^n\right]^m \\ &= \theta_r + (\theta_s - \theta_r)/\left[1 + \left(\frac{\Delta T}{\Delta T_{\mathrm{m}}}\right)^n\right]^m\end{aligned} \tag{11}$$

where ΔT_m is the thawing temperature depression (K). For the sake of convenience in numerical calculations, the temperature range of the SFCC can be extended to positive temperatures as follows,

Table 3
Input Parameter Values for Determining the Supercooling Degree

Parameter	Symbol	Value	Unit
Avogadro's constant	N_A	6.02×10^{23}	1/mol
Volume of a water molecule in an ice embryo	Ω_s	2.99×10^{-29}	m^3
Latent heat of water freezing	L_{wi}	6.01×10^{3}	J/mol
Surface free energy between ice and liquid	σ_{il}	3×10^{-2}	J/m^2
Boltzmann constant	K	1.38×10^{-23}	J/K
Nucleation rate factor	K	10^{36}–10^{42}	1/(m^3·s)

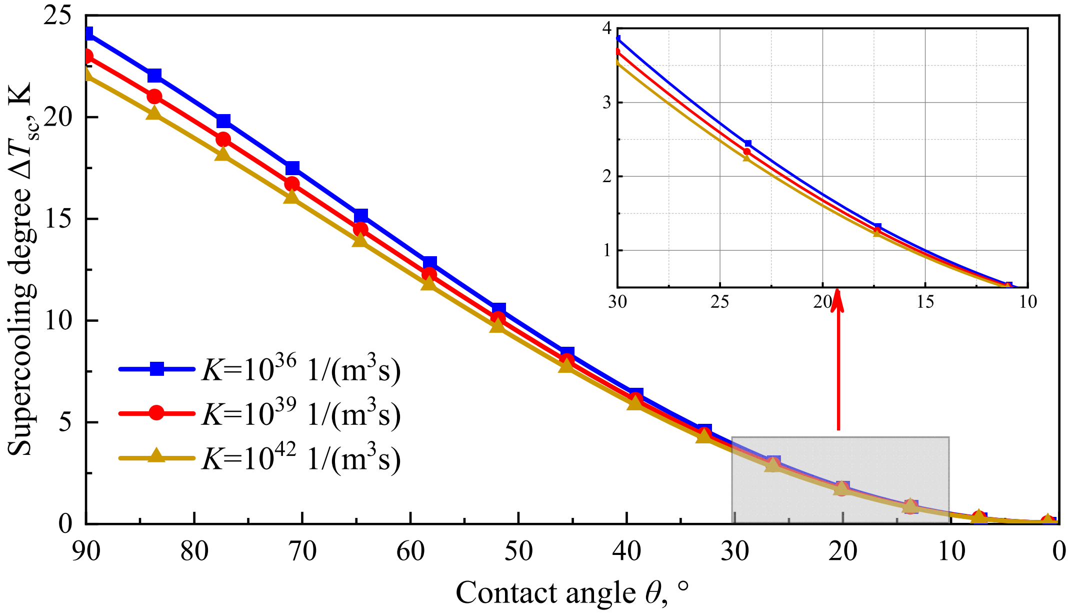

Figure 12. Variation of ΔT_{sc} with θ for different values of K.

$$\theta_{\mathrm{uT}} = \theta_r + (\theta_s - \theta_r) / \left[1 + \left(\frac{\Delta T}{\Delta T_m} H(\Delta T)\right)^n\right]^m \tag{12}$$

where $H(x)$ represents the Heaviside function, which takes 0 for $x < 0$ and 1 for $x \geq 0$.

3.2.3. The SFCC During the Freezing Branch

Based on the SFCC during the thawing branch, the SFCC for the freezing branch can be established by considering hysteretic behavior at different stages: the initial phase change stage, rapid phase change stage, and residual stable stage.

During the initial phase change stage, the soil temperature is between T_m and T_{sc}, and the SFCC remains horizontal. This phenomenon is primarily attributed to supercooling, which causes the initial freezing temperature to lag behind the thawing process by ΔT_{sc},

$$\theta_{\mathrm{uF}} = \theta_r + (\theta_s - \theta_r) / \left[1 + \left(\frac{\Delta T - \Delta T_{\mathrm{sc}}}{\Delta T_m} H(\Delta T - \Delta T_{\mathrm{sc}})\right)^n\right]^m \tag{13}$$

During the rapid phase change stage, the soil temperature is below T_{sc} and the SFCC experiences a rapid decrease. This phenomenon can be explained by the Gibbs-Thomson effect, wherein pores greater than r_{sc} freeze during the thawing process at T_{sc}. However, during the freezing process, supercooling suppresses the freeing of pores within the range of r_0 to r_{sc}. Once the temperature falls below T_{sc}, the previously suppressed pores freeze rapidly, along with smaller pores, resulting in a higher freezing rate compared to the thawing rate during this stage.

In the freezing process represented by Equation 13, pores with sizes ranging from r_0 to r_{sc} are assumed to freeze within the temperature range of T_{sc} to $T_{\mathrm{sc}} - \Delta T_{\mathrm{sc}}$ at the same rate as the thawing process. To account for the faster freezing rate observed during this stage, the error function (erf) is introduced to modify Equation 13.

$$\begin{cases} \theta_{\mathrm{uF}} = \theta_r + (\theta_s - \theta_r) / \left[1 + \left[\dfrac{[\Delta T - \Delta T_{\mathrm{sc}}[1 - \mathrm{CDF}(T)]] H(\Delta T - \Delta T_{\mathrm{sc}})}{\Delta T_m}\right]^n\right]^m \\ \mathrm{CDF}(T) = \dfrac{1}{2}\left(1 - \mathrm{erf}\left(\dfrac{T - \left(T_f - \dfrac{\Delta T_{\mathrm{sc}}}{2}\right)}{\sqrt{2} \cdot \dfrac{\sqrt{2}\,\Delta T_{\mathrm{sc}}}{8}}\right)\right) \end{cases} \tag{14}$$

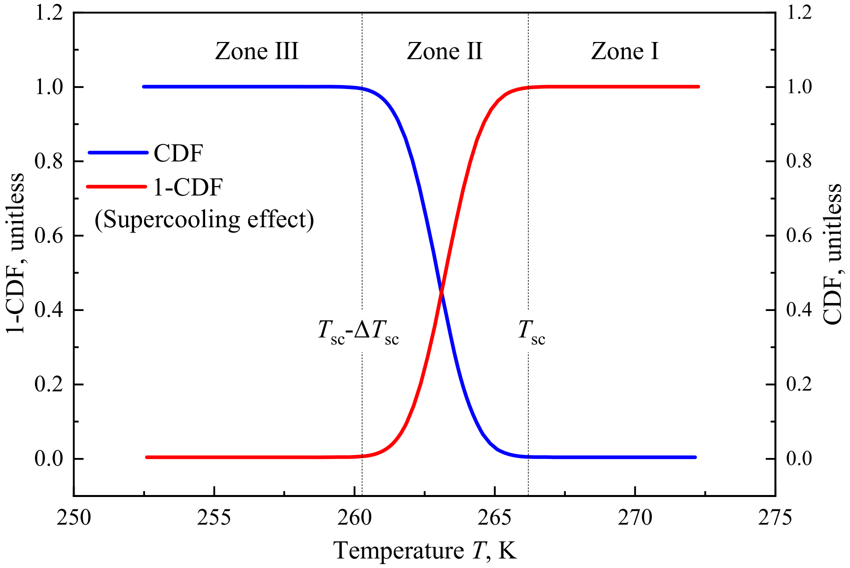

Figure 13. Variations of the CDF and supercooling effect in terms of the temperature.

where CDF(T) represents the cumulative distribution function of the standard normal distribution (Lu, 2016). The expression $T_c = T_f + \Delta T_{sc}/2$ denotes the mean temperature, and the term $\sigma_c = \sqrt{2}\Delta T_{sn}/8$ signifies the standard deviation. The term (1-CDF) represents the rapid freezing induced by supercooling. The variations of CDF and supercooling effect in terms of the temperature are presented in Figure 13.

During the residual stable stage, the influence of supercooling diminishes, resulting in minimal hysteresis in the freezing and thawing of adsorbed water (Overloop & Vangerven, 1993; C. Wang et al., 2018).

Therefore, Equations 12 and 14 represent the SFCC expressions considering freezing-thawing hysteresis. The model contains four parameters: m, n, ΔT_m, and ΔT_{sc}. The first three parameters are the same throughout the freezing and thawing process and can be determined by fitting measured data from the thawing process. The

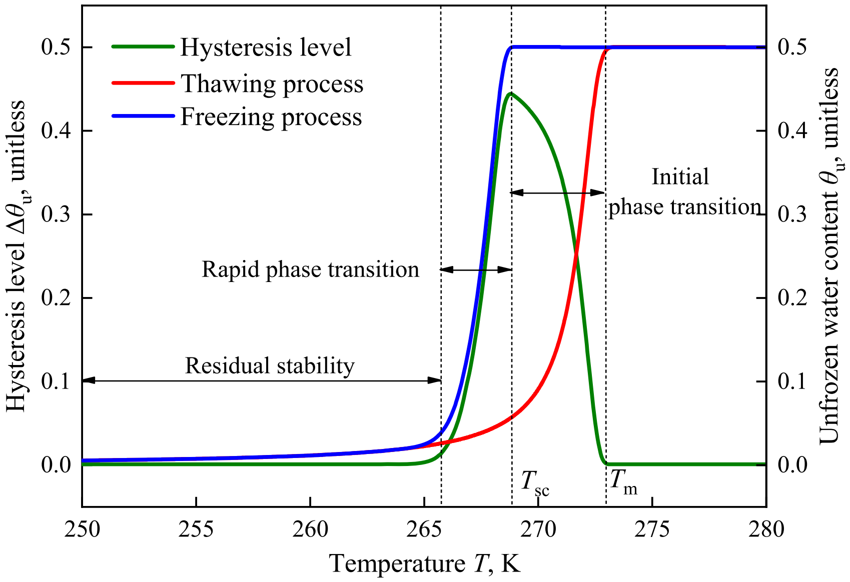

Figure 14. Variations of the unfrozen water content and hysteresis level in terms of the temperature ($\Delta T_m = 1$ K, $n = 3.0$, $m = 0.5$, $\theta_s = 0.5$, $\theta_r = 0$, and $\theta = 32°$).

Table 4
Physical Properties of the Soils in Some Works

			Component proportion			
Soil type	Porosity (/)	Dry density (g/cm^3)	Sand (%)	Silt (%)	Clay (%)	Reference
Lafayette silty clay	0.41	1.93	20	58	22	Dillon and Andersland (1966)
Humus-based soil	0.51	/	/	/	/	Sparrman et al. (2004)
Toronto silty clay	0.32	1.92	3	81	16	Ren and Vanapalli (2019)
Toronto lean clay	0.32	1.96	31	50	19	

parameter ΔT_{sc} can be determined by Equation 6. Taking the given factors: $\Delta T_m = 1$ K, $n = 3.0$, $m = 0.5$, $\theta_s = 0.5$, $\theta_r = 0$, and $\theta = 32°$, the calculation results of the proposed model are presented in Figure 14.

3.3. Model Validation

Experimental data from both this study and relevant literature are chosen to validate the performance of the proposed model. In this study, cases 4, 8, and 12 are selected for model justification. In previous literature, Dillon and Andersland (1966) measured the SFCC of non-expansive silty clay in the Indiana Lafayette area using the Adiabatic Calorimetry technique. Sparrman et al. (2004) employed 2H NMR to measure NMR signal intensity changes in humus-based soil with 51% initial water content in a southwestern Swedish karst landscape, where the signal intensity can be converted into unfrozen water content to obtain SFCC data. Ren and Vanapalli (2019) utilized the frequency domain reflectometry technique to measure the SFCCs of Toronto silty clay and Toronto lean clay in Canada. The physical factors of these four sets of soils from the selected literature are presented in Table 4.

According to the existing literature, various representations of water content exist, such as volumetric water content, mass water content, and saturation. For the purpose of comparison, this study uniformly converts these representations to unfrozen water saturation (S_{u}), which is defined as the ratio of liquid water volume (V_w) to pore volume (V_v). To further verify the performance of the proposed model, two existing models from the literature were selected for comparison. These include the analogous model proposed by Y. Zhou et al. (2019) based on SWCC hysteresis and the thermodynamic model proposed by Petrov and Furó (2009). The SFCC during the thawing branch is unified by Equation 12, allowing the hysteretic theory proposed by the above literature to be expressed in the form of SFCC, as summarized in Table 5.

Figure 15 shows the comparison between the prediction results of the three models and the experimental data from this study. The parameters m, n, ΔT_m, and S_r are determined by fitting the measured data during the thawing branch using Equation 12, as listed in Table 6. The parameter θ of the proposed model is determined through least-square fitting within the suggested range for soil types in Section 3.1. The parameter λ of Petrov and Furó (2009) is determined by fitting the measured data. As can be observed, the proposed model better captures the hysteretic behavior at all three stages, particularly during the initial phase change and rapid phase change stages. Comparing

Table 5
The Model Expressions of Freezing-Thawing Hysteresis

Reference	Model expression	Relevant parameter
Zhou et al. (2019)	$\begin{cases} S_{\text{uT}} = S_r + (1 - S_r)/\left[1 + \left(\dfrac{\Delta T}{\Delta T_m} H(\Delta T)\right)^n\right]^m \\ S_{\text{uF}} = 1 - (1 - S_{\text{uT}})^2 \end{cases}$	S_{uT} and S_{uF} are the unfrozen water saturation for the thawing and freezing process; S_r is the residual unfrozen water saturation
Petrov and Furó (2009)	$\begin{cases} S_{\text{uT}} = S_r + (1 - S_r)/\left[1 + \left(\dfrac{\Delta T}{\Delta T_m} H(\Delta T)\right)^n\right]^m \\ S_{\text{uF}} = S_r + (1 - S_r)/\left[1 + \left(\dfrac{\Delta T}{\Delta T_m/\lambda} H(\Delta T)\right)^n\right]^m \end{cases}$	λ is the ratio of the melting point reduction value to the freezing point reduction value, $\lambda = 2/3$ when the soil pore is spherical, $\lambda = 1/2$ when the pore is cylindrical, and $\lambda = 0$ when the pore is flat

the SFCCs of the three soils in Figure 15, it is found that T_m gradually decreases from sand to clay. This is attributed to the absence of supercooling during the thawing process, and T_m correlates with pore size. Additionally, the predicted curves for sand using the proposed model in Figure 15a exhibit nearly parallel behavior during the rapid phase change stage, whereas the slopes of SFCCs during freezing for silt and fat clay in Figures 15b and 15c exhibit a substantial increase compared to thawing. This observation is consistent with the experimental findings. The obtained results reveal that the consideration of the rapid phase change stage by the proposed model is reasonable.

Figure 16 shows the comparison between the predicted results and the measured data from the literature. The SFCCs predicted by the proposed model agree well with the experimental data. Despite all four soils being fine-grained, their rapid phase change stages are different. For Lafayette silty clay and Humus-based soil in Figures 16a and 16b, the rapid freezing stage is nearly parallel to the thawing stage. In contrast, Toronto silty clay and Toronto lean clay in Figures 16c and 16d show a significantly steeper slope during the rapid freezing stage compared to the thawing stage. This behavior can be attributed to the pore size distribution reflected by the SFCC of the thawing branch. A steeper SFCC, indicative of a more concentrated pore size distribution, leads to a smaller influence of supercooling on the rapid freezing stage. The measured data near 273.15 K in Figure 16d reveals that the soil is in a supersaturated or undersaturated state, which deviates from the predicted curve. This discrepancy may arise from differences in water content at the TDR probe location and the initial uneven water distribution. Such issues can be avoided by employing non-destructive testing techniques like NMR (Teng, Kou, et al., 2020). The measurement methods selected in the literature are based on calorimetric, NMR, and time-domain reflection, and the proposed model demonstrates the capability to predict results across different measurement techniques, which indicates the wide applicability of the proposed model.

Figures 15 and 16 also present the comparison between the predictions of the proposed model and reference models. The model developed by Petrov and Furó (2009) exhibits overall good predictions for poorly graded sand and Lafayette silty clay but tends to overestimate the SFCCs of Hohhot silt, Humus-based soil, and Toronto lean clay. The main reason for this fact is attributed to the model's neglect of the impact of supercooling, considering only the temperature difference between freezing and thawing. The model proposed by Y. Zhou et al. (2019) predicts an apparent upward deviation of SFCC during freezing. This deviation arises from the fact that SWCC hysteresis, which primarily includes pore blocking, contact angle hysteresis, and residual gas (Zhai et al., 2020), may not be directly applicable to SFCC hysteresis. SFCC hysteresis involves not only fluid flow but also thermodynamic factors such as the nucleation barrier (Wettlaufer & Worster, 2006). The substantial difference between these hysteresis mechanisms makes it challenging to directly apply SWCC hysteresis models to SFCC hysteresis models. Table 7 provides the correlation coefficients (R^2) between the predicted values of the different models and measured data. The proposed model consistently provides better predictions than existing models. This superiority is attributed to the fact that the proposed model combines the advantages of both the nucleation barrier and fluid flow, rather than relying solely on a single factor.

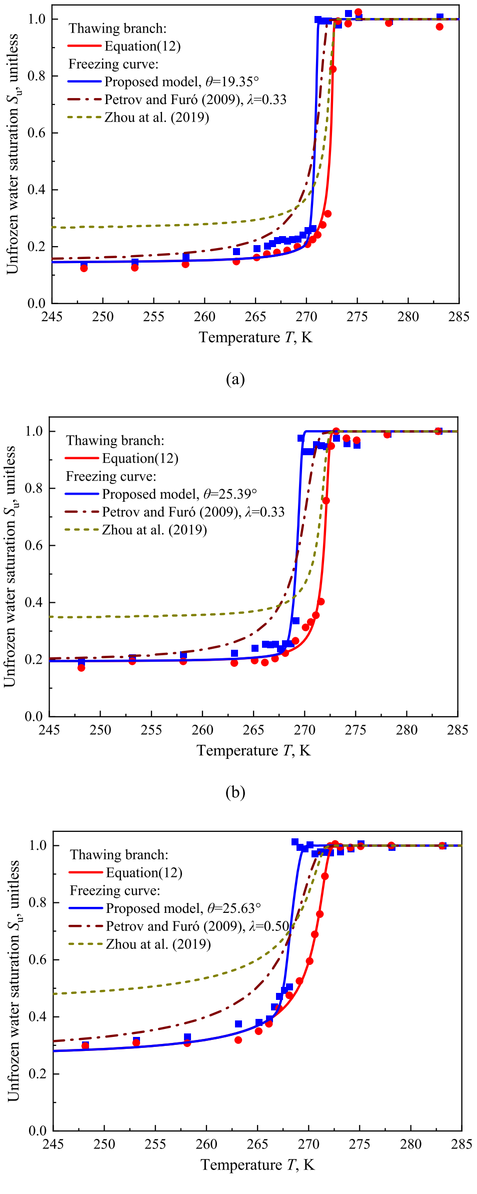

(a)

(b)

(c)

Figure 15. Comparison of the predicted and measured SFCCs for different soil types: (a) Poorly graded sand, (b) Silt, and (c) Fat clay (note: markers present the measured data, whereas the curves illustrate the proposed model predictions).

4. Conclusions

To investigate the freezing-thawing hysteretic behavior of soil, this study performs a series of laboratory tests by using NMR techniques. The experimental results reveal hysteresis during the main freezing-thawing process,

Table 6
Parameter Values of the Soil Freezing Characteristic Curve Model for the Thawing Branch

Soil type	T_m	n	m	S_r
Poorly graded sand	272.72	10.00	0.13	0.144
Silt	272.32	5.62	0.32	0.191
Fat clay	271.62	4.80	0.23	0.248
Lafayette silty clay	272.73	3.00	0.48	0.48
Humus-based soil	273.14	1.80	0.25	0.026
Toronto silty clay	271.10	1.70	1.06	0.23
Toronto lean clay	271.40	6.52	0.16	0.21

while it is negligible during the scanning freezing-thawing process. The obtained results are indicative of the fact that supercooling is the primary cause of freezing-thawing hysteresis. The effect of supercooling on hysteresis is theoretically examined, thus a novel model for freezing-thawing hysteresis is established.

The laboratory test results shed light on the mechanism of the freezing-thawing hysteretic behavior of soils. A distinct lag during freezing compared to thawing is observed, accompanied by a noticeable accelerated decline in the freezing curve. This disparity is attributed to the inhibitory effect of supercooling on pore water freezing. Once supercooling ends, the inhibited pore water freezes rapidly. The results indicate that supercooling controls freezing-thawing hysteresis. The study further reveals that increasing dry density weakens the degree of unfrozen water hysteresis, whereas growing the initial water content leads to lower supercooling temperatures and more pronounced freezing-thawing hysteresis.

The SFCC tests with various temperature modes are conducted to investigate the distinctions between SFCC hysteresis and SWCC hysteresis. The SFCCs in the main process rarely have parallel characteristics, and the scanning curves closely track the main thawing branch. Notably, freezing-thawing hysteresis during the scanning process is minimal, with a hysteretic level not exceeding 0.1. This phenomenon starkly contrasts with the approximate parallelism of the SWCCs observed during the wetting-drying process. These findings challenge

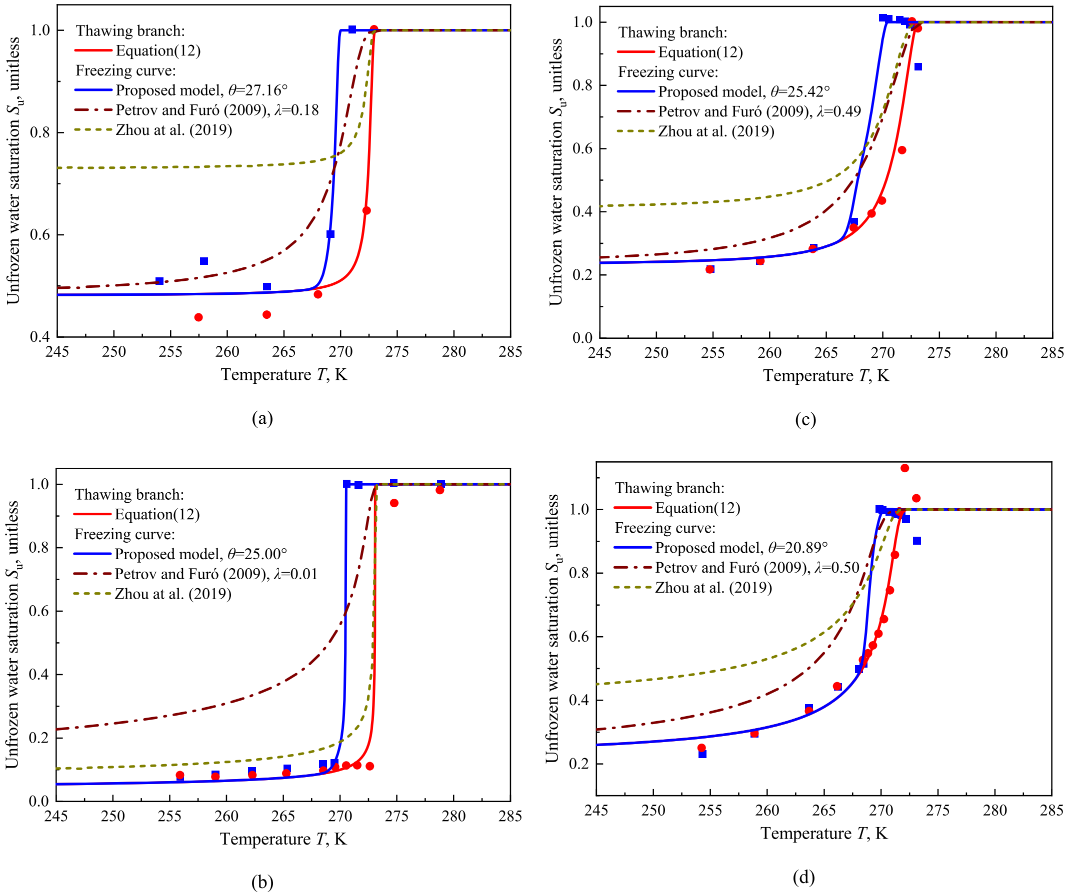

(a) (c)

(b) (d)

Figure 16. Comparison of the predicted and measured SFCCs for different soil types: (a) Lafayette silty clay, (b) Humus-based soil, (c) Toronto silty clay, and (d) Toronto lean clay (note: markers present the measured data, whereas the curves illustrate the proposed model predictions).

Table 7
The R^2 of Various Freezing-Thawing Hysteresis Models

Soil type	Zhou et al. (2019)	Petrov and Furó (2009)	Proposed model
Poorly graded sand	0.719	0.907	0.989
Silt	0.634	0.881	0.974
Fat clay	0.700	0.848	0.963
Lafayette silty clay	/	0.840	0.971
Humus-based soil	0.404	0.684	0.997
Toronto silty clay	0.752	0.836	0.976
Toronto lean clay	0.700	0.814	0.985

prevailing theories rooted in SWCC hysteresis, such as the ink bottle effect, as insufficient to explain SFCC hysteresis. Instead, supercooling emerges as the primary driver of freezing-thawing hysteresis.

A mathematical relation between supercooling degree and contact angle is derived based on the sub-stable heterogeneous nucleation theory. By considering the effects of supercooling on freezing-thawing hysteresis in the initial phase change, rapid phase change, and residual stability stages, a novel freezing-thawing hysteretic model is developed. The proposed model combines the influences of both the nucleation barrier and fluid flow, with a simple form and clear physical meaning. It agrees well with the measured data and demonstrates a better performance in predicting the supercooling stage and rapid freezing stage compared to previous models.

Appendix A

The free energy change (ΔG) induced by the ice embryo formation is stated by:

$$\Delta G = \Delta G_v + \Delta G_s = \Delta g V_i + \sigma_{il} A_{il} + (\sigma_{si} - \sigma_{sl}) A_{si} \tag{A1}$$

$$\Delta g = -\frac{L_{wi}}{N_A \Omega_s} \frac{\Delta T}{T_{\text{eq}}} \tag{A2}$$

Based on the mechanical equilibrium at the junction of the three phases, the relationship between θ and σ_{xy} can be expressed as follows,

$$\cos\theta = -\frac{\sigma_{si} - \sigma_{sl}}{\sigma_{il}} \tag{A3}$$

The volume of the ice embryo and the surface area of each contact surface are calculated as,

$$V_i = \frac{\pi r_{\text{i}}^2}{3}(2 + \cos\theta)(1 - \cos\theta)^2 \tag{A4}$$

$$\begin{cases} A_{il} = 2\pi r_i^2 (1 - \cos\theta) \\ A_{si} = \pi (r_i \sin\theta)^2 = \pi r_i^2 \left(1 - \cos\theta^2\right) \end{cases} \tag{A5}$$

By substituting Equations A3–A5 into Equation A1, the specific expression for ΔG is derived as,

$$\Delta G = \left(\frac{\pi}{3} {r_i}^3 \Delta g + \pi {r_i}^2 \sigma_{il}\right)(2 + \cos\theta)(1 - \cos\theta)^2 \tag{A6}$$

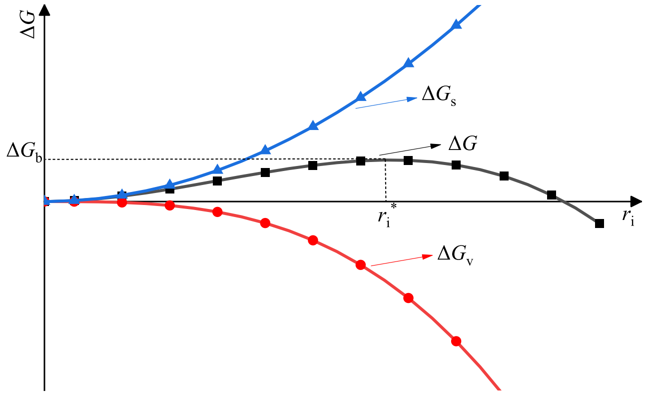

Figure A1. Variation of the free energy as a function of the ice embryo size.

The relationship between ΔG and r_i based on Equation A6 is presented in Figure A1. As r_i increases, ΔG initially rises and then decreases, reaching its maximum value (ΔG_{max}) at the critical radius (r_i*) of the ice embryo, representing the nucleation barrier.

Thermodynamic theory suggests that under isothermal and isobaric conditions, spontaneous reactions proceed from a high free energy state to a lower one. For ice embryos smaller than r_i*, the system free energy grows with radius, resulting in an endothermic process, causing these embryos to diminish until they disappear gradually. Conversely, for ice embryos larger than r_i*, the system free energy reduces with radius, indicating an exothermic process, allowing the larger ice embryos to stably grow into condensation nuclei.

The nucleation energy required to overcome the nucleation barrier, denoted by ΔG_b corresponding to the critical radius r_i*, can be determined by finding the extreme value of Equation A6, that is, $d\,(\Delta G)/dr_i = 0$. Therefore,

$$r_i{}^* = -\frac{2\sigma_{il}}{\Delta g} \tag{A7}$$

$$\Delta G_b = \frac{16}{3}\frac{\pi\sigma_{il}^3}{\Delta g^2}\frac{(2+\cos\theta)(1-\cos\theta)^2}{4} \tag{A8}$$

By substituting Equation A2 into Equation A1, ΔG_b can be rewritten as,

$$\Delta G_{\text{b}} = \frac{16}{3}\pi\sigma_{il}^3\left(\frac{N_{\text{A}}\Omega_{\text{s}}T_{\text{eq}}}{L_{\text{wi}}\Delta T}\right)^2 f(\theta) \tag{A9}$$

Data Availability Statement

The test data for the SFCC in this research were sourced from Dillon and Andersland (1966), Sparrman et al. (2004), and Ren and Vanapalli (2019), accessible via the following DOIs: https://doi.org/10.1139/t66-007, https://doi.org/10.1021/es0493695, and https://doi.org/10.2136/vzj2018.10.0185. All the results data utilized in the present study have been thoroughly documented and are incorporated within the manuscript, including its tables and figures. The referenced documents and associated data are publicly available and have been deposited on Zenodo (https://doi.org/10.5281/zenodo.10612282).

Acknowledgments
This research was supported by the National Natural Science Foundation of China (No. 52178376), National Key R&D Program of China (No. 2022YFB2603301), Natural Science Foundation of Hunan Province (2022JJ10076).

References

Amankwah, S. K., Ireson, A. M., Maulé, C., Brannen, R., & Mathias, S. A. (2021). A model for the soil freezing characteristic curve that represents the dominant role of salt exclusion. *Water Resources Research*, *57*(8), e2021WR030070. https://doi.org/10.1029/2021WR030070

Anderson, R., Tohidi, B., & Webber, J. B. W. (2009). Gas hydrate growth and dissociation in narrow pore networks: Capillary inhibition and hysteresis phenomena. *Geological Society London Special Publications*, *319*(1), 145–159. https://doi.org/10.1144/SP319.12

Bachmann, J., Woche, S. K., Goebel, M. O., Kirkham, M. B., & Horton, R. (2003). Extended methodology for determining wetting properties of porous media. *Water Resources Research*, *39*(12), SBH111–SBH1114. https://doi.org/10.1029/2003WR002143

Bittelli, M., Flury, M., & Campbell, G. S. (2003). A thermodielectric analyzer to measure the freezing and moisture characteristic of porous media. *Water Resources Research*, *39*(2), SBH111–SBH1110. https://doi.org/10.1029/2001WR000930

Black, P. B., & Tice, A. R. (1989). Comparison of soil freezing curve and soil water curve data for Windsor sandy loam. *Water Resources Research*, *25*(10), 2205–2210. https://doi.org/10.1029/WR025i010p02205

Brooks, R. H., & Corey, A. T. (1964). Properties of porous media affecting fluid flow. *Journal of the Irrigation and Drainage Division Proceedings of the American Society of Civil Engineers*, *92*(2), 61–88. https://doi.org/10.1061/JRCEA4.0000425

Caicedo, B. (2017). Physical modelling of freezing and thawing of unsaturated soils. *Géotechnique*, *67*(2), 106–126. https://doi.org/10.1680/jgeot.15.P.098

Coussy, O., & Fen-Chong, T. (2005). Crystallization, pore relaxation and micro-cryosuction in cohesive porous materials. *Comptes Rendus-Mécanique*, *333*(6), 507–512. https://doi.org/10.1016/j.crme.2005.01.005

Devoie, É. G., Gruber, S., & McKenzie, J. M. (2022). A repository of measured soil freezing characteristic curves: 1921 to 2021. *Earth System Science Data*, *14*(7), 3365–3377. https://doi.org/10.5194/essd-14-3365-2022

Dillon, H. B., & Andersland, O. B. (1966). Predicting unfrozen water contents in frozen soils. *Canadian Geotechnical Journal*, *3*(2), 53–60. https://doi.org/10.1139/t66-007

Fabbri, A., Fen-Chong, T., Azouni, A., & Thimus, J.-F. (2009). Investigation of water to ice phase change in porous media by ultrasonic and dielectric measurements. *Journal of Cold Regions Engineering*, *23*(2), 69–90. https://doi.org/10.1061/(ASCE)0887-381X(2009)23:2(69)

Fen-Chong, T., & Fabbri, A. (2005). Freezing and thawing porous media: Experimental study with a dielectric capacitive method. *Comptes Rendus-Mécanique*, *33*(5), 425–430. https://doi.org/10.1016/j.crme.2005.01.007

Fletcher, N. H. (1958). Size effect in heterogeneous nucleation. *The Journal of Chemical Physics*, *29*(3), 572–576. https://doi.org/10.1063/1.1744540

Fredlund, D. G., & Xing, A. (1994). Equations for the soil-water characteristic curve. *Canadian Geotechnical Journal*, *31*(4), 521–532. https://doi.org/10.1139/t94-061

Fu, Y., Liao, H., Chai, X., & Lv, L. L. (2021). A hysteretic model considering contact angle hysteresis for fitting soil-water characteristic curves. *Water Resources Research*, *57*(4), 1–46. https://doi.org/10.1029/2019WR026889

Gharedaghloo, B., Berg, S. J., & Sudicky, E. A. (2020). Water freezing characteristics in granular soils: Insights from pore-scale simulations. *Advances in Water Resources*, *143*, 103681. https://doi.org/10.1016/j.advwatres.2020.103681

Koopmans, R. W. R., & Miller, R. D. (1966). Soil freezing and soil water characteristic curves. *Soil Science Society of America Journal*, *30*(6), 680–685. https://doi.org/10.2136/sssaj1966.03615995003000060011x

Kowalenko, C. G., & Babuin, D. (2013). Inherent factors limiting the use of laser diffraction for determining particle size distributions of soil and related samples. *Geoderma*, *193–194*, 22–28. https://doi.org/10.1016/j.geoderma.2012.09.006

Kulkarni, G., Fan, J., Comstock, J. M., Liu, X., & Ovchinnikov, M. (2012). Laboratory measurements and model sensitivity studies of dust deposition ice nucleation. *Atmospheric Chemistry and Physics*, *12*(16), 7295–7308. https://doi.org/10.5194/acp-12-7295-2012

Kurylyk, B. L., & Watanabe, K. (2013). The mathematical representation of freezing and thawing processes in variably-saturated, non-deformable soils. *Advances in Water Resources*, *60*, 160–177. https://doi.org/10.1016/j.advwatres.2013.07.016

Kurz, W., & Fisher, D. J. (1992). *Fundamentals of solidification*. Trans Tech Publications Ltd.

Liu, Z., & Yu, X. (2013). Physically based equation for phase composition curve of frozen soils. *Transportation Research Record: Journal of the Transportation Research Board*, *2349*(1), 93–99. https://doi.org/10.1016/j.coldregions.2014.09.003

Lu, N. (2016). Generalized soil water retention equation for adsorption and capillarity. *Journal of Geotechnical and Geoenvironmental Engineering*, *10*(142), 04016051. https://doi.org/10.1061/(ASCE)GT.1943-5606.0001524

Morishige, K., & Kawano, K. (1999). Freezing and melting of water in a single cylindrical pore: The pore-size dependence of freezing and melting behavior. *The Journal of Chemical Physics*, *10*(10), 4867–4872. https://doi.org/10.1063/1.478372

Mullin, J. W. (2001). *Crystallization*. Butterworth Heinemann.

Nishimura, S., Okajima, S., Joshi, B. R., Higo, Y., & Tokoro, T. (2021). Volumetric behaviour of clays under freeze-thaw cycles in a mesoscopically uniform element. *Géotechnique*, *71*(12), 1150–1164. https://doi.org/10.1680/jgeot.20.P.047

Nishimura, S., & Wang, J. (2019). A simple framework for describing strength of saturated frozen soils as multi-phase coupled system. *Géotechnique*, *69*(8), 659–671. https://doi.org/10.1680/jgeot.17.P.104

Overloop, K., & Vangerven, L. (1993). Freezing phenomena in adsorbed water as studied by NMR. *Journal of Magnetic Resonance - Series A*, *101*(2), 179–187. https://doi.org/10.1006/jmra.1993.1028

Pardo Lara, R., Berg, A. A., Warland, J., & Parkin, G. (2021). Implications of measurement metrics on soil freezing curves: A simulation of freeze-thaw hysteresis. *Hydrological Processes*, *35*(7), 1–17. https://doi.org/10.1002/hyp.14269

Petrov, O. V., & Furó, I. (2009). NMR cryoporometry: Principles, applications and potential. *Progress in Nuclear Magnetic Resonance Spectroscopy*, *54*(2), 97–122. https://doi.org/10.1016/j.pnmrs.2008.06.001

Qian, M., & Ma, J. (2009). Heterogeneous nucleation on convex spherical substrate surfaces: A rigorous thermodynamic formulation of Fletcher's classical model and the new perspectives derived. *The Journal of Chemical Physics*, *130*(21), 214709. https://doi.org/10.1063/1.3146810

Ren, J., & Vanapalli, S. K. (2019). Comparison of soil-freezing and soil-water characteristic curves of two Canadian soils. *Vadose Zone Journal*, *18*(1), 180185–180214. https://doi.org/10.2136/vzj2018.10.0185

Ren, J., & Vanapalli, S. K. (2020). Effect of freeze-thaw cycling on the soil-freezing characteristic curve of five Canadian soils. *Vadose Zone Journal*, *19*(1), e20039. https://doi.org/10.1002/vzj2.20039

Saberi, P. S., König, C., & Meschke, G. (2021). A hysteresis model for the unfrozen liquid content in freezing porous media. *Computers and Geotechnics*, *137*, 104298. https://doi.org/10.1016/j.compgeo.2021.104298

Sheng, D., Zhang, S., Niu, F., & Cheng, G. (2014). A potential new frost heave mechanism in high-speed railway embankments. *Géotechnique*, *64*(2), 144–154. https://doi.org/10.1680/geot.13.P.042

Sparrman, T., Öquist, M., Klemedtsson, L., Schleucher, J., & Nilsson, M. (2004). Quantifying unfrozen water in frozen soil by high - Field ^{2}H NMR. *Environmental Science and Technology*, *38*(20), 5420–5425. https://doi.org/10.1021/es0493695

Style, R. W., Peppin, S. S., Cocks, A. C., & Wettlaufer, J. S. (2011). Ice-lens formation and geometrical supercooling in soils and other colloidal materials. *Physical Review E*, *84*(4), 041402. https://doi.org/10.1103/PhysRevE.84.041402

Sun, K., & Zhou, A. (2021). A multisurface elastoplastic model for frozen soil. *Acta Geotechnica*, *16*(11), 3401–3424. https://doi.org/10.1007/s11440-021-01391-7

Sun, Z., & Scherer, G. W. (2010). Effect of air voids on salt scaling and internal freezing. *Cement and Concrete Research*, *40*(2), 260–270. https://doi.org/10.1016/j.cemconres.2009.09.027

Teng, J., Kou, J., Yan, X., Zhang, S., & Sheng, D. (2020). Parameterization of soil freezing characteristic curve for unsaturated soils. *Cold Regions Science and Technology*, *170*, 102928. https://doi.org/10.1016/j.coldregions.2019.102928

Teng, J., Liu, J., Zhang, S., & Sheng, D. (2020). Modelling frost heave in unsaturated coarse-grained soils. *Acta Geotechnica*, *15*(11), 3307–3320. https://doi.org/10.1007/s11440-020-00956-2

Teng, J., Liu, J., Zhang, S., & Sheng, D. (2022). Frost heave in coarse-grained soils: Experimental evidence and numerical modelling. *Géotechnique*, *73*(12), 1100–1111. https://doi.org/10.1680/jgeot.21.00182

Teng, J., Zhong, Y., Zhang, S., & Sheng, D. (2021). A mathematic model for the soil freezing characteristic curve: The roles of adsorption and capillarity. *Cold Regions Science and Technology*, *181*, 103178. https://doi.org/10.1016/j.coldregions.2020.103178

Tian, H., Wei, C., Wei, H., & Zhou, J. (2014). Freezing and thawing characteristics of frozen soils: Bound water content and hysteresis phenomenon. *Cold Regions Science and Technology*, *103*, 74–81. https://doi.org/10.1016/j.coldregions.2014.03.007

To, P., Scheuermann, A., & Williams, D. J. (2018). Quick assessment on susceptibility to suffusion of continuously graded soils by curvature of particle size distribution. *Acta Geotechnica*, *13*(5), 1241–1248. https://doi.org/10.1007/s11440-017-0611-8

Van Genuchten, M. T. (1980). A closed-form equation for predicting the hydraulic conductivity of unsaturated soils. *Soil Science Society of America Journal*, *44*(5), 892–898. https://doi.org/10.2136/sssaj1980.03615995004400050002x

Wan, X., Liu, E., & Qiu, E. (2020). Study on ice nucleation temperature and water freezing in saline soils. *Permafrost and Periglacial Processes*, *32*(1), 119–138. https://doi.org/10.1002/ppp.2081

Wan, X., Pei, W., Lu, J., Qiu, E., Yan, Z., Pirhadi, N., & Zhu, J. (2022). Analytical model to predict unfrozen water content based on the probability of ice formation in soils. *Permafrost and Periglacial Processes*, *33*(4), 436–451. https://doi.org/10.1002/ppp.2167

Wang, C., Lai, Y., Yu, F., & Li, S. (2018). Estimating the freezing-thawing hysteresis of chloride saline soils based on the phase transition theory. *Applied Thermal Engineering*, *135*, 22–33. https://doi.org/10.1016/j.applthermaleng.2018.02.039

Wang, Y., & Hu, L. (2023). A theoretical model of soil freezing characteristic curve considering the freezing of adsorbed water and capillary water. *Water Resources Research*, *59*(7), e2023WR034662. https://doi.org/10.1029/2023WR034662

Watanabe, K., & Osada, Y. (2017). Simultaneous measurement of unfrozen water content and hydraulic conductivity of partially frozen soil near 0°C. *Cold Regions Science and Technology*, *142*, 79–84. https://doi.org/10.1016/j.coldregions.2017.08.002

Wettlaufer, J. S., & Worster, M. G. (2006). Premelting dynamics. *Annual Review of Fluid Mechanics*, *38*(1), 427–452. https://doi.org/10.1146/annurev.fluid.37.061903.175758

Ying, S., Zhou, F., & Wen, T. (2021). Study on characteristic temperatures of cooling saline soil. *Polish Journal of Environmental Studies*, *30*(2), 1893–1901. https://doi.org/10.15244/pjoes/126502

Zhai, Q., Rahardjo, H., Satyanaga, A., Dai, G., & Du, Y. (2020). Estimation of the wetting scanning curves for sandy soils. *Engineering Geology*, *272*, 105635. https://doi.org/10.1016/j.enggeo.2020.105635

Zhang, M., Zhang, X., Lai, Y., Lu, J., & Wang, C. (2020). Variations of the temperatures and volumetric unfrozen water contents of fine-grained soils during a freezing-thawing process. *Acta Geotechnica*, *15*(3), 595–601. https://doi.org/10.1007/s11440-018-0720-z

Zhou, J., Meng, X., Wei, C., & Pei, W. (2020). Unified soil freezing characteristic for variably - Saturated saline soils. *Water Resources Research*, *56*(7), e2019WR026648. https://doi.org/10.1029/2019WR026648

Zhou, Y., Zhou, J., Shi, X., & Zhou, G. (2019). Practical models describing hysteresis behavior of unfrozen water in frozen soil based on similarity analysis. *Cold Regions Science and Technology*, *157*, 215–223. https://doi.org/10.1016/j.coldregions.2018.11.002